Journal of Materials Chemistry C

Advancing the next generation nanolithography with infiltration synthesis of hybrid nanocomposite resists

Journal:	*Journal of Materials Chemistry C*
Manuscript ID	TC-COM-06-2019-002974.R1
Article Type:	Communication
Date Submitted by the Author:	05-Jul-2019
Complete List of Authors:	Tiwale, Nikhil; Brookhaven National Laboratory Subramanian, Ashwanth ; Stony Brook University, Materials Science and Chemical Engineering; Brookhaven National Laboratory, Center for Functional Nanomaterials Kisslinger, Kim; Brookhaven National Laboratory, Center for Functional Nanomaterials Lu, Ming; Brookhaven National Lab, 2Center for Functional Nanomaterials Kim, Jiyoung; University of Texas at Dallas, Materials Science and Engineering Stein, Aaron; Brookhaven National Laboratory Nam, Chang-Yong; Brookhaven National Laboratory, Center for Functional Nanomaterials

SCHOLARONE™
Manuscripts

COMMUNICATION

Advancing the next generation nanolithography with infiltration synthesis of hybrid nanocomposite resists

Received 00th January 20xx,
Accepted 00th January 20xx

DOI: 10.1039/x0xx00000x

Nikhil Tiwale,[a] Ashwanth Subramanian,[b] Kim Kisslinger,[a] Ming Lu,[a] Jiyoung Kim,[c] Aaron Stein,[a] and Chang-Yong Nam [a,b]*

Organic-inorganic hybrid resists are emerging as effective way of addressing stringent process requirements for aggressive down-scaling of semiconducting devices. However, hybrid resists generally require complex chemical synthesis while being predominantly negative-tone with high dose requirement. For positive-tone processes and high-aspect-ratio pattern transfer, resist choices are limited to costly, non-hybrid alternatives, whose etch resistance is still inferior compared with hybrid resists. Here, we demonstrate a novel hybrid positive-tone resist platform utilizing simple ex-situ vapor-phase inorganic infiltration into standard resist materials. A model system based on poly(methyl methacrylate) (PMMA) thin film hybridized with aluminum oxide has been demonstrated for electron-beam lithography patterning, featuring fully controllable critical exposure dose, contrast, and etch resistance. The hybrid resist not only achieves contrast as high as ~30, six-fold enhancement over standard PMMA but also enables Si nanostructures with resolution down to ~30 nm and aspect ratio as high as ~17, owing to Si etch selectivity enhanced to ~70, with estimated achievable maximum of ~300, far exceeding known commercial positive-tone resist systems. The easy implementabilility, combined with versatile ex-situ control of resist characteristics, makes this hybrid resist synthesis approach uniquely suited for addressing the resist performance and high throughput required for advanced nanolithography techniques, such as extreme ultraviolet lithography, potentially.

Introduction

Lithography has played a crucial role in the gigantic processing power that semiconductor industry has conjured by shrinking down electronic device feature sizes to the sub-10 nm length scale. So far, the photoresists that allowed reproducible fabrication of such a small length-scales have been largely carbon-based, chemically amplified resists (CAR). However, more recently, organic-inorganic hybrid resists are gaining significant attention, in order to satisfy the stringent requirements imposed by the aggressive device-scaling.[1] Until now the industry-scale lithography has been dependent on 193 nm immersion lithography (193-i),[2] with further scaling imparted by clever engineering tricks such as directed self-assembly[3,4] and multi-patterning.[1,5] The lithography techniques capable of directly patterning sub-10 nm-scale resolution such as electron beam lithography (EBL) and extreme ultraviolet (EUV) lithography are currently being pursued for application into the high-volume manufacturing (HVM). However, in order to transfer these high-resolution patterns into required substrates with high aspect ratios, hybrid resists must provide a key solution.[1,6]

Performance of a lithographic tool inevitably depends on the resists capable of instilling the required nanopatterns. To this end, the currently existing resists face a number of challenges. Typically, at the resist thicknesses that had been used for previous technology nodes, the high-resolution patterns undergo pattern collapse, necessitating decrease in the resist thickness, where such small linewidths could be realized.[7] Consequently, the resist patterns do not survive the plasma-etch time required to transfer them into the substrate with required high aspect ratio.[1] In order to balance the resolution-etch selectivity trade-off, thin layer imaging (TLI) and related approaches have been exploited, such as top surface imaging (TSI) via silylation,[8–16] use of bilayer resist consisting of Si-containing top layer,[17] selective area atomic layer deposition (ALD),[18] ion beam implantation,[19–21] and hard mask underlayer.[17] Nowadays, multilayer stacks have been in use to increase the pattern transfer selectivity, but its implementation requires multiple number of processing steps which negatively affects the throughput and cost.

The hybrid resists offer an elegant solution over this conundrum. The increased mechanical strength due to the

[a] *Center for Functional Nanomaterials, Brookhaven National Laboratory, Upton, New York 11973, United States.*
**E-Mail: cynam@bnl.gov*
[b] *Department of Materials Science and Chemical Engineering, Stony Brook University, Stony Brook, New York 11794, United States.*
[c] *Department of Materials Science and Engineering, University of Texas at Dallas, Richardson, Texas 75080, United States.*
† Electronic Supplementary Information (ESI) available: See DOI: 10.1039/x0xx0000

inorganic component helps in reducing pattern collapse. Moreover, the enhanced robustness, imparted by the inorganic entities, provides higher etch resistance; allowing a deep, high-aspect-ratio etching into the substrate. In addition, for EUV lithography, where absorption of the EUV radiation primarily takes place at the atomic level, inclusion of specific elements into the resist matrix can improve energy absorbed by the resist and, thus, the throughput.[1] To this end, a number of inorganic containing hybrid resist strategies are being actively investigated for EUV resist application, such as those based on nanoparticles, [6,22–27] oxalates,[28–31] and oxocages.[32,33]

One of the seminal works on metal-containing electron beam (e-beam) resists was conducted by Webb and Hatzakis of IBM using metal methacrylates.[34] However, this approach has remained a relatively unpopular choice because of high exposure dose necessary to generate solubility contrast. Another early approach of incorporating inorganic entity into the resist utilized a copolymer of methyl methacrylate (MMA) and 3-triethoxysilylpropyl methacrylate (ESPMA). Only 1 – 10 % addition of ESPMA lead to 4 – 10 times etch resistance improvement.[35] Saifullah and Welland et.al. have investigated e-beam resists containing a number of metals and associated metal oxides based on such as Al, Ti, Hf, Zr, Zn, Ni, Cu.[36–45] While an excellent linewidth resolution was demonstrated, their sensitivity was extremely low, thus, requiring high exposure dose for generating the patterns. Grenci, Zanchetta, Brusatin et.al. have demonstrated a highly etch-resistant molecular resist (containing organo-phenylsilane derivatives) with moderate exposure dose;[46–49] which was later also co-opted by Cattoni et. al. by using less toxic silane derivatives.[50] Despite demonstrating Si etch selectivity up to 100:1 for this resist system, susceptibility of the silane groups to ambient humidity poses limitation on their long-term shelf-life.[50] More recent works have tried to utilize resists containing metal peroxide sulfates,[51,52] metal sulfonates,[53] metal containing polymers (MCP)[54] and organosilicates.[55,56] Hydrogen silsesquioxane (HSQ), a Si-containing caged monomer-based resist, has been the most widely used inorganic based resist for EBL. However, similar to most hybrid resists, HSQ is also a negative-tone resist with a high exposure dose requirement.[57–60] Moreover, most of these hybrid resists are chemically synthesized using processes that would require highly skilled workforce. These resists are also generally hard to remove and leave behind residue after lithography.

Meanwhile, there are only a few variants of positive-tone e-beam resists with high etch resistance that have been explored. The most popularly employed resist choices for plasma etch based patterning include copolymer resists such as ZEP520A (Zeon Corp.),[61,62] CSAR62 (ALLRESIST GmbH)[63,64] or a photoacid generator (PAG) containing CAR - UV series (Shipley/Dow Chemical).[65] It must be noted that all these resists have proprietary compositions with relatively high associated cost. While these resists show moderately improved etch resistance, being inherently organic, they still suffer from typical limitations of carbon-based resists detailed earlier. To this end, the reports of positive-tone, metal containing hybrid resists are particularly lacking.

In this study, we demonstrate a novel hybrid positive-tone e-beam resist system, developed entirely using readily available standard material systems and fabrication tools. Our process does not involve any kind of complex chemical synthesis, making it easy to implement with custom protocols. Moreover, since our resist system is based on existing resist materials with ex-situ processing used to modify the resist prior to exposure, issues such as substrate adhesion, which may occur with resists synthesized by complex chemistry, are completely avoided; whereas, since the ex-situ processing only requires standard fabrication tool, the same principles can be easily implemented for other metals and metal oxides to achieve specific performance. A key novelty in our resist system is the inherent controllability of various resist parameters, such as sensitivity (D_{50}), contrast (γ) as well as plasma etch resistance, as per the need of the user and the end application. Within this resist platform, we report hybrid nanocomposite resists with contrast, γ, ranging from 2 to 30 by carefully controlling the amount of inorganic (AlO_x). Using our hybrid resist with thickness as small as ~60 nm, we were able to etch Si features down to ~30 nm linewidth and very high aspect ratio of ~17. The etch selectivity of the corresponding resist formulation for cryogenic Si etching was estimated to be as high as ~70, which is a fourteen-fold increase in the etch selectivity of the original (pre-hybridization) organic resist and even over five-fold higher than the resist of choice for etch processes, ZEP. Based on measured etch rates of resist infiltrated with higher number of infiltration cycles, we also estimate selectivity in excess of 300.

Poly(methyl methacrylate), more commonly known as PMMA, is by far the most widely used EBL resist.[66–71] Its popularity, in part, stems from the associated simple nature of the chemistry involved and its ubiquitous, low-cost availability as well as its long-term shelf life. It is a positive-tone resist, which has also been demonstrated to show ~1 nm pattering resolution, the highest resolution reported for any EBL resist.[72] However, one major negative side for the conventional PMMA resist is that it lacks the plasma etch resistance,[73] which has led the EBL users to rather costly alternative resists such as ZEP, CSAR. Our PMMA-based hybrid resist tackles this very drawback with a low-cost synthesis technique. Even in the semiconductor industry, which has been heavily dependent on 193-i lithography, copolymers of methacrylate derivatives have been the workhorse for HVM.[2,74–76] Consequently, the hybridized resist system reported here can have a lasting impact by easily adopting it for a number of different advanced lithography techniques.

This journal is © The Royal Society of Chemistry 2019

Please do not adjust margins

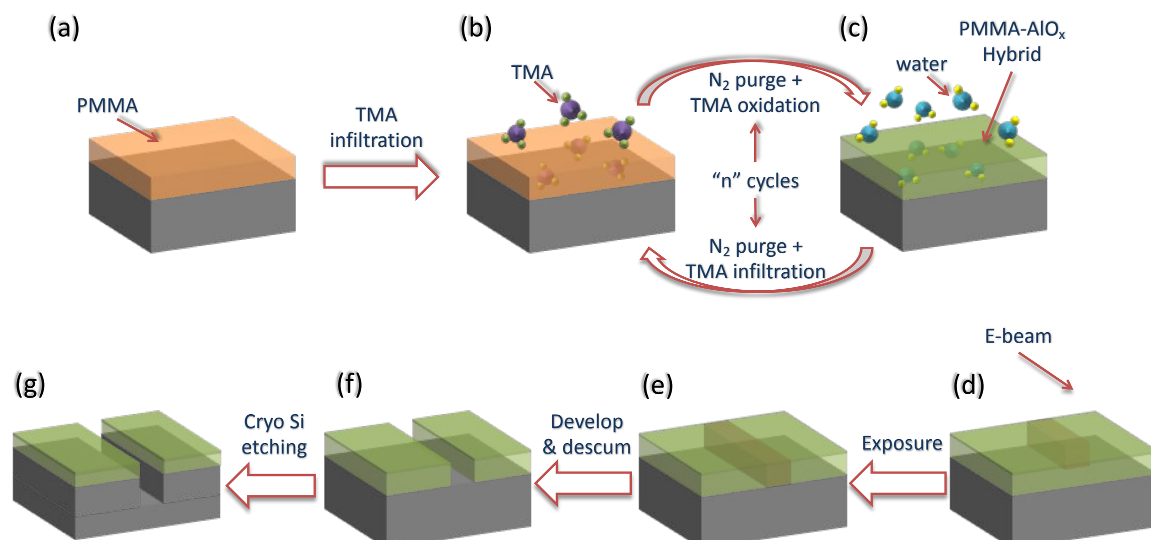

Fig. 1 Schematic representation of the process flow followed during the current study (a) PMMA 950 A2 was spin coated on cleaned Si substrates with 7500 rpm for 60 sec resulting into ~60 nm PMMA film. During the infiltration process alternating half-cycles of (b) TMA infiltration and (c) water infiltration are repeated for given number of times in order to synthesize ex-situ processed hybrid resist composition. The sample with hybrid resist is then subjected to e-beam exposure (d); and resulting modified resist with specific patterned areas (e) is then developed in 1:3 MIBK:IPA solution for 45 sec followed by 15 sec IPA rinse to acquire patterned substrate (f). After an appropriate descum process, the patterned substrate is then subjected to cryogenic Si etch process at -100 °C using combination of SF_6-O_2 gas mixture to transfer the pattern into the Si substrate (g).

We have employed a recently developed vapor-phase hybridization technique called infiltration synthesis or vapor-phase infiltration.[77–79] The technique utilizes atomic layer deposition (ALD) tool, a very common thin-film deposition equipment found in almost every micro-nano-fabrication facility. The substrate is first coated with required thickness of PMMA resist using simple spin-coating technique and then loaded into the ALD chamber maintained at a moderate temperature (85 °C), below the glass transition temperature of PMMA. During the infiltration process, Al precursor, trimethylaluminum (TMA), is first introduced into the chamber for a stipulated amount of time while the chamber is isolated from the pump. At the end of the required time, TMA is then purged out of the chamber. This constitutes the first half of an infiltration cycle. In the subsequent half-cycle, an oxidizing precursor, typically water (H_2O), is introduced in a similar way to oxidize the infiltrated TMA, and then purged out. These two combined half-cycles constitute a full infiltration cycle and are repeated several times to achieve required amount of infiltration of AlO_x in the PMMA matrix (Fig. 1a-c). While the infiltration synthesis technique has previously been reported, we have used a modified version of the same, a micro-dose protocol, where the precursor (or oxidant) is pulsed for multiple number of times during the half cycle exposure to promote more homogeneous, higher amount of infiltration as we have reported recently.[80]

Although the infiltration synthesis process is based on the ALD tool and uses ALD precursors, the underlying mechanism is vastly different from the normal ALD. In a typical material deposition by ALD, TMA molecules are adsorbed on the substrate surface to form a monolayer during the first half-cycle. This adsorbed layer is subsequently oxidized to form a monolayer of AlO_x, during the second half-cycle. As the cycle is repeated for a given number of times, AlO_x film is slowly grown on the top of the substrate. In a nutshell, the ALD process is governed by the surface adsorption process. On the contrary, during the infiltration half-cycle, which is typically much longer compared to ALD half-cycle (i.e., a few minutes vs. a few seconds), TMA diffuses into the molecular-scale pores available in the PMMA matrix and attaches itself to the carbonyl groups inside the polymeric chains.[78,81] During the water half-cycle, these TMA molecules are then oxidized to form Al-OH groups. On repeating the infiltration cycle, AlO_x grows on top of the initial Al-OH groups. Ultimately, the total number of applied infiltration cycles thus govern the amount of inorganic or the degree of hybridization of the polymeric matrix.[77]

Results and discussion

We first studied the basic characteristics of our hybrid resist sensitivity (S) and contrast (γ), where the resist formulation was altered with different number of AlO_x infiltration cycles ranging from 0 to 8. We demonstrate excellent controllability of S and γ based on the amount of infiltration. Particularly, in comparison to original PMMA resist, we have achieved almost an order of magnitude increase in the contrast. Fig. 1d-f depict the general process of EBL which employed for resist patterning. Fig. 2a-c illustrate a typical electron dose test carried out in the form of an exposure matrix for uninfiltrated, 4-cycle infiltrated, and 8-cycle infiltrated PMMA, respectively, depicted as the height maps acquired using atomic force microscopy (AFM). The exposure dose in these tests was increased from left to right and top to bottom (The exposure dose used at each array position are included in Table S1). The reproducibility of the exposure response of the synthesized hybrid resist was verified using dark-field optical microscopy of the exposure matrix, as shown

Please do not adjust margins

in Fig. S1, across three or more number of samples. Consequently, AFM analysis was conducted on representative sample for each infiltration condition, and the acquired AFM height maps for all the infiltration conditions investigated in this study are provided in Fig. S2. From the AFM maps themselves, it can be observed that the electron dose required to cause a solubility change within the resist and consequently develop positive-tone patterns, increases with the increasing number of infiltration cycles and, thus, the amount of incorporated inorganic content. Based on the prior understanding of the infiltration mechanism, the infiltrated AlO_x growing within the polymer matrix may be causing the internal crosslinking among the polymer chains. Similarly, the enhancement in the resist contrast can also be noticed from the AFM maps; the thickness change within the exposed areas is initially gradual for the hybrid resists with low numbers of infiltration cycles. However, as the infiltrated inorganic content is increased, a more abrupt change in the height of the exposed regions can be seen, clearly suggesting an increase in the contrast of the resist for higher numbers of infiltration cycles.

Fig. 2d quantifies the exposure matrix height data in the form of post-development remnant height percentage in the exposed region against the exposure dose on a semi-logarithmic scale. All resist profiles show a typical sigmoidal distribution, where the exposure dose required to remove the 50% resist height is quantified as the critical dose (D_{50}). We find that the sigmoidal contrast curves shift towards higher exposure doses with increased infiltration, implying the requirement of higher exposure dose to clear the resist from the exposed region. The slopes of the sigmoidal contrast curves also can be observed to become steeper with increased infiltration cycles, signifying the increment in the resist contrast, γ, which can be quantified using the expression,[82]

$$\gamma = \frac{1}{\log_{10}\left(\frac{D_{100}}{D_0}\right)}$$

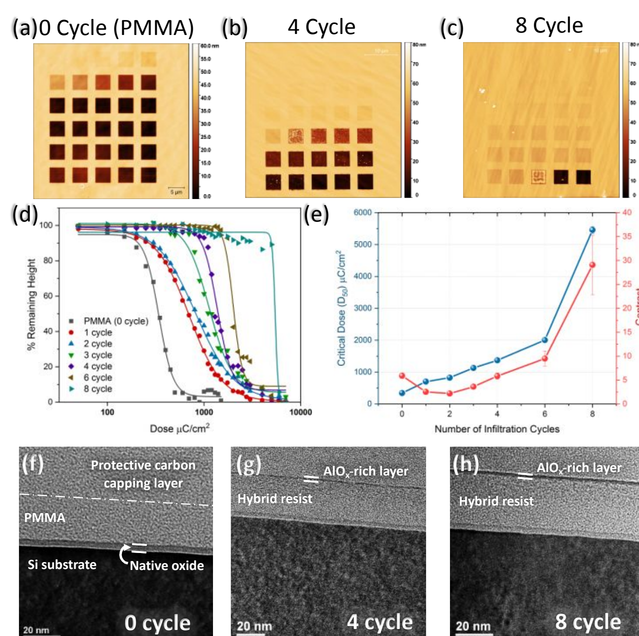

Fig. 1 AFM height maps of exposure dose matrix patterned as per the dose array illustrated in Table S1 on (a) PMMA (0-cycle infiltration) (b) 4-cycle infiltrated hybrid resist and (c) 8-cycle infiltrated hybrid resist. (d) Exposure dose response curves for all the rest formulations studied illustrated by plotting %remaining height vs. corresponding exposure dose; heights acquired from the AFM maps. (e) Evolution of critical dose (D_{50}) and contrast (γ) with increasing number of infiltration cycles. Bright-field cross-sectional TEM images of (f) pure PMMA (0-cycle infiltration) (g) 4 cycle infiltrated and (h) 8 cycle infiltrated resist showing increasing amount of AlO_x into the PMMA matrix, along with growing thickness of the AlO_x-rich top layer.

where D_0 is the onset dose and D_{100} is the dose to clear the resist. The estimated values of critical dose and contrast are plotted against the number of infiltration cycles in Fig. 2e. A nearly monotonous increase in the critical dose is seen with increased infiltration. The contrast values on the other hand show only a small change until 4 cycles, and rapidly increases to ~ 30 for resists with 8 cycles of infiltration, which is almost a six-fold increase compared to starting PMMA resist.

In order to investigate the origin for this unexpected contrast enhancement, we conducted the cross-sectional transmission electron microscopy (TEM) on the hybrid resist thin films after different amounts of AlO_x infiltration, and the acquired images are shown in Fig. 2f-h. A dense, AlO_x-rich thin layer can be seen to have formed at the top surface of the infiltrated resist, which seems to be getting thicker with increasing amount of infiltration. The formation of such a thin top layer would explain the contrast enhancement in the case of highly infiltrated hybrid resist. Since this top layer can initially retard the developer solution from entering the interior of exposed regions, only relatively small quantity of resist would be removed at lower doses, causing an insignificant change in the resist thickness. Such a negligible thickness change would continue until the dose is significantly increased such that a more significant amount of resist under the dense layer starts becoming dissolved. When the dose is finally over the critical value, the underlying resist would be completely removed along with the thin top AlO_x-rich layer, consequently rendering the entire exposed region cleared. During the height measurement,

This journal is © The Royal Society of Chemistry 2019

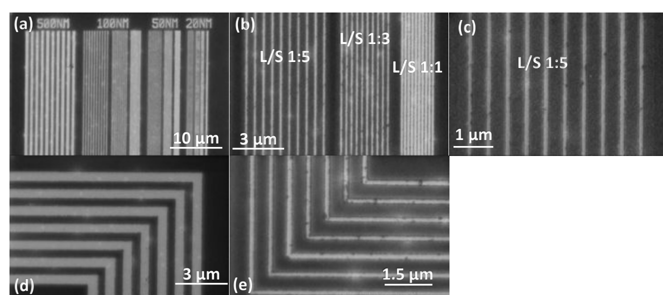

Fig. 3 (a) Low magnification scanning electron microscopy (SEM) image of nanopatterns with LW and spacings. (b) High-magnification SEM micrograph of 100 nm LW patterns with spacing varying from 100 nm to 500 nm. (c) Magnified in image of 1:5 Line/Space patterns of 100 nm LW. (d) Elbow patterns of 500 nm half-pitch and (e) 100 nm LW elbow patterns with 500 nm pitch.

this is recorded as a sudden removal of all the resist in the exposed region close to a particular exposure dose and translates into a near ideal, high contrast. It also should be noted that the formation of such a top dense layer is typically seen in previous reports of vapor-phase infiltration under the limited diffusion of AlO_x precursor into the polymer matrix.[77,83] However, due to the use of modified micro-dose protocol, we were able to infuse AlO_x much more efficiently throughout the polymer matrix, as indicated by the negligible AlO_x segregation in the PMMA matrix observed in the TEM images, and the thin top layer is likely generated by the adsorption-driven material deposition via the standard ALD on the resist surface, which becomes dominant as the molecular pores are being clogged with repeated infiltration cycles.

As the semiconductor industry is marching towards higher and higher device density, the requirement of robust high-resolution patterns is quintessential for advanced nodes. Here, we have used the 4-cycle AlO_x-infiltrated PMMA resist composition and have successfully demonstrated a number of sub-micrometre periodic line and elbow patterns down to 50 nm. Fig. 3a presents a low-magnification scanning electron microscopy (SEM) image of nanopatterns with different linewidth (LW) and spacings. Fig. 3b depicts high-magnification SEM micrographs of 100 nm LW patterns with different periodicity, whereas Fig. 3c is a magnified image of 1:5 line/space (L/S) patterns of 100 nm LW. Furthermore, elbow patterns of 500 nm half-pitch and 100 nm LW elbow patterns with 500 nm pitch are shown in Fig. 3d,e, respectively. We note that, after the development a descum step was necessary to clear up remaining residue. While a 10 sec O_2 reactive ion etching (RIE) at 100 mTorr pressure and 20 W RF power as a descum protocol is quite commonly used in the case of PMMA based nanopatterning, we used a 5 sec dip into 0.26 N tetramethyl ammonium hydroxide (TMAH) to remove the inorganic residue prior to O_2 RIE descum step. While the primary purpose of TMAH dip is to clear residues from the developed region, we note that it may also dissolve the thin surface AlO_x-rich layer on top of unpatterned resist areas. However, the brief TMAH dip does not affect AlO_x retained within the polymer matrix and, thus, the enhanced etch resistance of hybrid resist. With the help of these high-resolution hybrid resist patterns with high etch resistance,

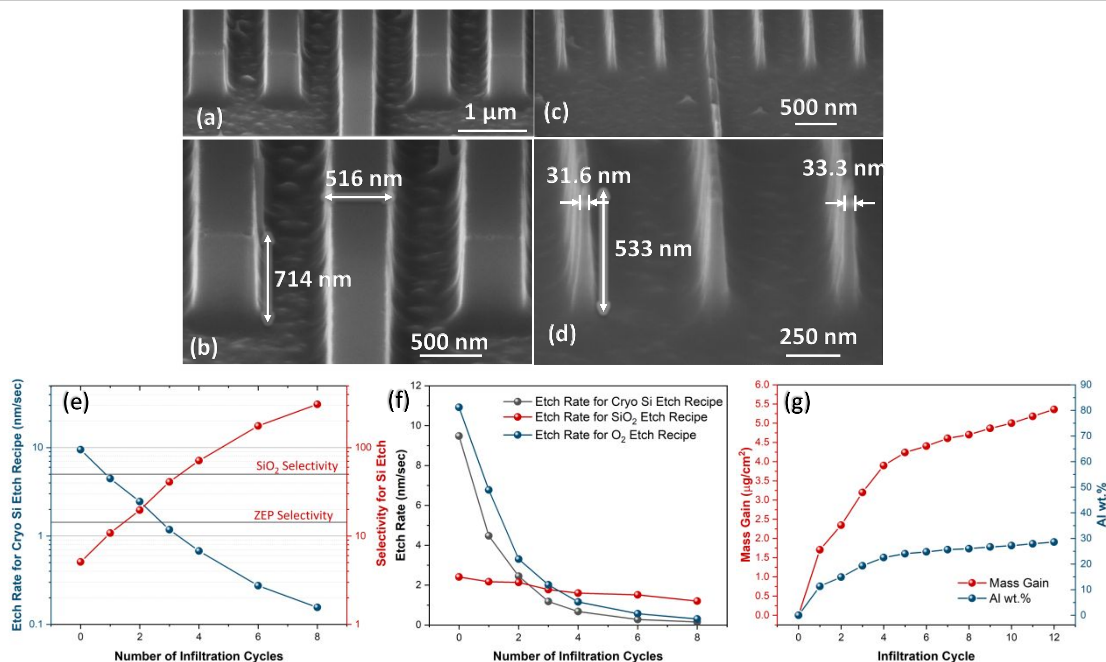

Fig. 2 60°-tilted SEM images of the high aspect ratio Si nanostructures etched using 4-cycle infiltrated PMMA-AlO_x hybrid resist. (a) Low-magnification and (b) high-magnification SEM images of 500 nm half-pitch high density (1:1 L/S) patterns. (c) Low-magnification and (d) high-magnification SEM images of high-resolution high-aspect-ratio Si nanostructures patterned at 500 nm pitch. (e) Variation in the resist etch rate for cryo-Si etch process and selectivity for Si etching for resist composition consisting different number of infiltration cycles. Notably the 2-cycle infiltrated resist surpasses selectivity of ZEP and 4-cycle infiltration leads to selectivity higher than SiO_2 hard mask. (f) Comparison of etch rate decrease with the increasing number of infiltration cycles; while moderate etch rate decrease is seen in physical etch dominated SiO_2 etch recipe, the decrease in etch rate for etch recipes with higher chemical component is relatively greater. (g) Mass gain per area (left axis) and Al wt.% (right axis) with increasing number of infiltration cycles estimated via QCM measurements.

This journal is © The Royal Society of Chemistry 2019

Please do not adjust margins

Table 1 Comparison of various EBL resist processes and their properties. SIS refers to sequential infiltration synthesis.

Resist	Lithography	Post Lithography Treatment	LW (nm)	Etched Depth (nm)	Aspect Ratio	Dose ($\mu C/cm^2$) [*J/cm^2]	Etch Recipe	Resist Etch Rate (nm/min)	Si Etch Rate (nm/min)	Selectivity with Si
PMMA [78,79]	EBL		20	10	0.5	~500	HBr	300	100	3
PMMA [79]	EBL	SIS	18	130	7.22		HBr	<4	100	>25
PMMA [78]	EBL	SIS	~150	1500	~10		HBr	~8	100	~12.5
ZEP520A [78]	EBL						HBr	100	100	1
ZEP520A [78]	EBL	SIS					HBr	20	100	5
Al-Si complex [48]	Soft X-ray (negative)	100 °C for 60 s	400	3300	8.5-17.5	20*	SF_6-C_4F_8-Ar	2.67	170	>60
Al-Si complex [56]	EBL 3kV (negative)		20	400	20	200-250	SF_6-C_4F_8-Ar	2.67	170	>100
Al-Si complex [46]	EBL (Dual) 30kV		<100, min 20	3000	>30	800	SF_6-C_4F_8-Ar	~1.7	170	100
HSQ[46]	EBL neg		10			5000	SF_6-C_4F_8-Ar		170	6
This work; 4-cycle hybrid	EBL 100kV		31.6	533	16.87	~2000	SF_6-O_2-Cryo	40.67	~2895	~71.2

ultimately, high-aspect-ratio Si patterns could be realized using the plasma-based Si etching processes as discussed below.

In order to transfer developed resist patterns, we have exploited the inductively coupled plasma (ICP)-RIE etching using SF_6/O_2-based fluorine chemistry, along with a cryogenic cooling of the substrate down to −100 °C (Fig. 1g). SF_6 provides very high isotropic etch rate with Si, quite often very hard to control by itself and leading to undercut or pattern broadening. However, such a detrimental sidewall etching can be avoided by inclusion of appropriate amount of O_2 into the gas mixture. O_2 forms a thin oxyfluoro-polymer (SiO_xF_y) layer as the etching progresses and protects the Si surface.[84,85] Although this could lead to a significant etch rate decrease, due to the ion bombardment directed by the RF bias, the polymer at the bottom of the trench is removed and the SF_6 etching can keep progressing at a rapid rate. Additionally, the cryogenic temperature plays a vital role in minimizing physical erosion of the resist, thus allowing deep high-aspect ratio Si etching.

We have utilized the 4-cycle infiltrated resist formulation to pattern Si nanostructures with very high aspect ratio of ~17 with LW of ~30 nm and depth in excess of 530 nm. Fig. 4a-d depicts 60°-tilted SEM images of the high aspect ratio Si structures patterned using 4-cycle infiltrated PMMA-AlO_x hybrid resist and the SF_6-based cryo-etch for merely 20 sec. Low- and high-magnification SEM images of 500 nm half-pitch, high-density patterns are shown in Fig. 4a,b, respectively, while the SEM images of higher-resolution Si structures using the resist patterned at 500 nm pitch are shown in Fig. 4c,d. The LW of ~31.6 nm and depth of 533 nm leading to the aspect ratio as high as 16.8 was thus achieved.

In an attempt to benchmark our resist's performance against previously reported resists, we have summarized key performance parameters in Table 1. While etched structures with aspect ratio as high as 100 have been previously reported by Brusatin et. al.,[46] it should be noted that the inorganic content infiltrated in our resist is significantly lower, and the infiltrated AlO_x has fundamentally altered the chemical nature of the PMMA resists generating a hybrid nanocomposite, which has in turn increased its robustness for plasma etching. Such an unprecedented enhancement of the polymer mechanical properties due to AlO_x-infiltration has also been previously reported in case of SU-8 resist.[86] Moreover, organo-silane chemistry based resists reported by Brusatin et. al. show susceptibility to ambient humidity,[50] which compromises their long-term shelf life. Tseng, Elam, Darling et. al., in their original reports demonstrating the process of infiltration synthesis for etch resistance improvement of patterned PMMA and ZEP resist structures, utilized infiltration *after initial patterning step*,[78,79] demonstrating Si etch selectivity over 25 for HBr chemistry.

In comparison, in our ex-situ-generated PMMA-AlO_x hybrid resists not only selectivity as high as ~309 is estimated, but also having pre-infiltrated resist imparts improved robustness and allows usability of rather thicker resist films without causing pattern collapse. The Si etch selectivity demonstrated by our process also surpasses routinely used resists ZEP (selectivity ~14.3 for our cryo Si recipe and ~1 for HBr chemistry[78]) as well as HSQ (~6 for SF_6-C_4F_8-Ar chemistry[46]; the detailed list of resists/hard mask tested in this study is provided in Table 2). Moreover, while we have utilized the hybrid resist with 4-cycle infiltration (selectivity ~70) for demonstrating nanostructures and pattern transfer, the extrapolation of measured resist etch rate data suggests that Si etch selectivity more than 300 should be achievable by further increasing the amount of infiltration up to 8 cycles. The variation in Si etch selectivity for our cryo etch process based on number of infiltration cycles is illustrated in Fig. 4e**.** The trend of selectivity improvement with increasing infiltration also demonstrates easy controllability of resist's

 This journal is © The Royal Society of Chemistry 2019

Please do not adjust margins

robustness for etching based processing. After merely 2-cycles of infiltration, the etch selectivity exhibited by the hybrid resist (~20) surpasses that of ZEP resist (~14.3), which, albeit being costly, is a popular choice for etching based pattern transfer. In a number of industrial processes, SiO_2 hard mask is employed between the resist and the Si substrate, in order to improve selectivity at the expense of a few additional steps.[79] It should be noted that our 4-cycle infiltrated hybrid resist formulation shows 40 % higher Si etch selectivity (~70) as compared to thermal SiO_2 (~50), thus removing the need for additional processing steps.

Table 2 Summary of measured resist/hard-mask etching rate for cryo-Si etching process and corresponding estimated selectivity for Si etch

Resist/hard mask material	Etch Rate (nm/min)	Selectivity with Si etching
SiO_2	58.0	49.9
ZEP520	202.2	14.3
PMMA	568.6	5.1
PMMA-AlO_x hybrid, 1 cycle	268.3	10.8
PMMA-AlO_x hybrid, 2 cycle	147.2	19.7
PMMA-AlO_x hybrid, 3 cycle	70.7	40.9
PMMA-AlO_x hybrid, 4 cycle	40.7	71.2
PMMA-AlO_x hybrid, 6 cycle	16.5	175.9
PMMA-AlO_x hybrid, 8 cycle	9.4	309.2

In order to elucidate the effect of hybridization on various aspects of ICP-RIE etching process, we selected three different etch recipes with each having different degrees of combined chemical and physical etching characteristics. Cryo-Si etch recipe, utilized for the aforementioned high aspect ratio Si etching, contains both physical and chemical components that play roles in the etching process. Pure O_2 etch is typically used predominantly for removing organic resist and proceeds via chemical route, whereas SiO_2 etch recipe majorly relies on the physical sputtering aspect. As depicted in Fig. 4f, for all three etching recipes, there is a decrease in the etching rate with increasing number of infiltration cycles. Interestingly though, the change in the etch rate for cryo-Si and O_2 etch recipes, is much more drastic compared to the observed change in the etch rate for SiO_2 etching recipe. This observation is rather surprising considering that the common predisposition behind the inclusion of inorganic components into the organic matrix is to improve their resistance to physical damage caused by sputtering when subjected to plasma. On the contrary, our hybrid resists seem to show comparatively higher chemical resistance than physical resistance, indicating that our process has altered the chemical nature of the original polymer matrix.

We further estimated the amount of AlO_x infiltrated into the PMMA matrix with the help of quartz crystal microbalance (QCM) measurements (temporal frequency variation shown in Fig. S3), and the resulting areal mass gain for different number of infiltration cycles is illustrated in Fig. 4g. It can be noticed that initially the mass gain rate is relatively high, but it starts decreasing as the infiltration cycles repeats. Such a trend in the mass gain behaviour is attributed to the fact that the number of reactive sites within the PMMA matrix decrease with each infiltration cycles and thus for higher cycles, the TMA molecule find insufficient reactive sites to form chemical bond. Additionally, the formation of thin top AlO_x-rich layer also should be contributing to the decreasing permeability of the TMA molecules. The evolution of Al wt.% with increasing number of infiltration cycles is also illustrated in Fig. 4g. It is noteworthy that almost ~30 wt.% of Al could be infiltrated into the PMMA matrix (at 12 cycles) with corresponding Al/C atomic ratio of ~0.3 (Fig. S4).

Controllability of the resist performance is a unique aspect of our resist system that makes it a versatile resist platform. Depending upon the end application in mind, the resist formulation could be easily altered to achieve an optimal performance out of the resist. For example, the cutting-edge Fin-FET based transistor architecture used in the latest processor chips requires patterning down to sub-10 nm with device height being ~50 nm. Low amount of infiltration can provide high throughput high resolution patterning with relatively low aspect ratio patterns, as needed in this case. On the other hand, the memory device industry is exploiting three-dimensional (3D) stacking of the memory cells in order to increase memory density, where rather lower LW resolution (~100 nm) suffices, but with the required etch depth as high as few micrometres. Increasing the amount of infiltration can give ultra-high contrast and extremely high aspect ratio with some decrease in the throughput and relatively lower resolution, which is quite suitable for the posed requirement.

While the current work has majorly focused on the EBL of the PMMA-AlO_x hybrid resist, our resist platform in principle can easily be adaptable for other advanced lithography techniques. Starting this year, a number of leading semiconductor manufacturers are embarking towards utilizing the EUV lithography (EUVL), which has been in the research pipeline for more than a decade. The EUVL, owing to its ultra-short wavelength, can pattern sub-10 nm structures in single exposures, which would obviate the need for multi-patterning strategies and decrease design complexity. The current understanding of the EUVL exposure mechanism in resists is that the interaction of EUV photons with resists gives rise to secondary photoelectrons that can carry out the solubility change within the resist.[1,87] Moreover, the absorption of EUV radiation is primarily realized by the component atoms, and thus the inclusion of specific elements in the resist formulation has significant impacts. For instance, metal atoms such as Al show relatively high EUV absorption, while metals like Sn can exhibit very high EUV absorption,[88,89] compared with carbon, hydrogen, and oxygen, the primary atomic components of pure organic resists, which have low EUV absorption. That said, although, the current study has primarily focused on AlO_x infiltration into the polymer matrix, the ease of processing and controllability of our hybrid resist make it a versatile, potential route towards generating organic-inorganic hybrid resists containing other metal and metal oxide systems[77,90–96] for high-throughput patterning of sub-10 nm structure with required

This journal is © The Royal Society of Chemistry 2019

Please do not adjust margins

high aspect ratios via EUVL. Moreover, we note that a further investigation into exploring resist and infiltration synthesis chemistries as well as developer chemistries and protocols may prove beneficial for optimizing key resist performance parameters such as sensitivity as well as line edge roughness (LER).

Conclusions

In summary, we have developed a new, high-performance, easy-to-access hybrid resist system, via the ex-situ infiltration synthesis process based only on existing standard materials and tools. Implementing our resist strategy with a representative system based on PMMA and AlO_x, we have achieved very high contrast of ~30 for EBL-based patterning, with a minor increase in required exposure dose, which is still similar to widely used negative-tone resist HSQ. Moreover, we have been able to demonstrate the fabrication of Si nanopatterns with high aspect ratio of ~17 owing to the etch selectivity value of ~71.2, much higher (5 – 14 times higher) than commonly used resist such as PMMA, ZEP and HSQ. Another four-fold increment in the selectivity (reaching >300) is also estimated for hybrid infiltrated with 8 infiltration cycles. By subjecting our resists to different plasma-RIE processes, we also uncovered unique enhancement in the chemical etch resistance. Since there is no complex underlying chemical synthesis requirement, the process is extremely easy to implement and modify. Versatile controllability of the generated hybrid resist performance is yet another highly desirable attribute, suitable for optimal process development as per the application demand. Moreover, with the industry advancing to EUVL for HVM, our technique should be also utilizable, with appropriate choices of infiltrated inorganic elements, towards achieving high throughput nanolithography for next generation electronics development.

Experimental Methods

Hybrid resist formulation by infiltration synthesis: Commercially available 2 wt.% PMMA (molecular weight 950,000 g/mol – MicroChem) in anisole was spin coated on cleaned silicon substrates at 7500 rpm for 60 sec, followed by 3 min baking at 180 °C hotplate to form ~60 nm film as measured by ellipsometry. The substrates with as spun PMMA film were then infiltrated at 85 °C with different AlO_x amount by varying the number of infiltration cycles from 1 – 12 using a commercial ALD system (Cambridge Nanotech Savannah S100). Each infiltration cycle consisted of TMA exposure for total 60 sec, during which TMA precursor was pulsed for 14 msec every 10 sec, followed by purging of the ALD chamber with 100 sccm N_2 for 2 min. Consequently, the substrates were exposed to water vapor for total 60 sec, while the 40 msec pulses were employed every 10 sec, followed by 2 min purge by 100 sccm N_2, completing the infiltration cycle.

EBL: E-beam exposure on the prepared samples was carried out using JEOL JBX-6300FS EBL system (100 kV). For the exposure matrix patterning typically 500 pA current was used to expose 5 μm square area with electron dose ranging from 50 $\mu C/cm^2$ to 7000 $\mu C/cm^2$ using a shot spacing of 8 nm. For exposing sub-micrometer scale features consisting of lines and elbow patterns 1 nA beam current and 4 nm shot spacing was used (exposure dose range differed for various formulations). After the exposure, samples were developed in methyl iso-butyl ketone (MIBK) solution in isopropyl alcohol (IPA) in the ratio of MIBK:IPA 1:3 for 45 sec followed by 15 sec rinse in IPA.

Dry etching: All ICP-RIE processing was conducted in Oxford Plasmalab 100. The plasma processing conditions are summarized in Table S2.

Electron microscopy characterization: SEM micrographs were acquired using Hitachi 4800 field-emission SEM. Cross-sectional TEM samples were prepared by the standard in-situ lift-out procedure using Ga ion milling in a focused ion beam system (FEI Helios 600 Nanolab). TEM images were taken using a JEOL JEM-1400 TEM at 120 kV. AFM characterization of the dose test measurements were carried out using Park NX20 AFM with PPP-NCHR tips.

Conflicts of interest

There are no conflicts to declare.

Acknowledgements

Authors thank Dr Xiao Tong for his assistance with AFM measurements and Dr Dmytro Nykypanchuk with ellipsometry measurements. The research was carried out at the Center for Functional Nanomaterials (CFN), Brookhaven National Laboratory (BNL), which is supported by the U.S. Department of Energy, Office of Basic Energy Sciences, under Contract No. DE-SC0012704.

References

1 S. Wang, L. Li, C. K. Ober, E. P. Giannelis, X. Liu and S. Pal, *Chem. Soc. Rev.*, 2017, **46**, 4855–4866.
2 E. P. Giannelis, M. Trikeriotis, R. Rodriguez, W. J. Bae, M. F. Zettel, C. K. Ober, E. Piscani and P. Zimmerman, *Adv. Resist Mater. Process. Technol. XXVI*, 2009, **7273**, 727326.
3 M. A. Morris, *Microelectron. Eng.*, 2015, **132**, 207–217.
4 J. Roberts, R. A. Griffiths, A. Vijayaraghavan, T. Thomson, A. Williams and C. Oakland, *J. Phys. D. Appl. Phys.*, 2013, **46**, 503001.
5 R. F. Pease and S. Y. Chou, *Proc. IEEE*, 2008, **96**, 248–270.
6 L. Li, S. Chakrabarty, K. Spyrou, C. K. Ober and E. P. Giannelis, *Chem. Mater.*, 2015, **27**, 5027–5031.
7 A. Tavakkoli K. G., S. N. Piramanayagam, M. Ranjbar, R. Sbiaa and T. C. Chong, *J. Vac. Sci. Technol. B, Nanotechnol. Microelectron. Mater. Process. Meas. Phenom.*, 2011, **29**, 011035.
8 M. A. Hartney, R. R. Kunz, D. J. Ehrlich and D. C. Shaver, in *Advances in Resist Technology and Processing VII*, ed. M. P. C. Watts, 1990, vol. 1262, p. 119.
9 J. W. Thackeray, *J. Vac. Sci. Technol. B Microelectron. Nanom. Struct.*, 1989, **7**, 1620.
10 M. Endo, I. Satou, H. Watanabe and H. Morimoto, *Microelectron. Eng.*, 2000, **53**, 485–488.
11 E. K. Pavelchek, *J. Vac. Sci. Technol. B Microelectron. Nanom. Struct.*, 1990, **8**, 1497.

This journal is © The Royal Society of Chemistry 2019

Please do not adjust margins

12 R. S. Hutton, *J. Vac. Sci. Technol. B Microelectron. Nanom. Struct.*, 1990, **8**, 1502.
13 B. Roland, *Microelectron. Eng.*, 1991, **13**, 11–18.
14 C. Pierrat, S. Tedesco, F. Vinet, T. Mourier, M. Lerme, B. Dal'Zotto and J. C. Guibert, *Microelectron. Eng.*, 1990, **11**, 507–514.
15 D. Kontziampasis, K. Beltsios, E. Tegou, P. Argitis and E. Gogolides, *J. Appl. Polym. Sci.*, 2010, **117**, 2189–2195.
16 K. Arshak, M. Mihov, A. Arshak, D. McDonagh, M. Pomeroy and M. Campion, *Microelectron. Eng.*, 2002, **61**–**62**, 783–791.
17 M. Ryoo, S. Shirayone, E. Yano, S. Okazaki and S. Kang, *Microelectron. Eng.*, 2002, **61**–**62**, 723–728.
18 A. Sinha, D. W. Hess and C. L. Henderson, *Electrochem. Solid-State Lett.*, 2006, **9**, G330.
19 P. A. F. Herbert, J. Braddell and S. Mackenzie, *Engineering*, 1994, **23**, 263–266.
20 F. E. Prins, J. Pfeiffer, S. Raible, D. P. Kern and V. Schurig, *Microelectron. Eng.*, 1998, **42**, 359–362.
21 K. Arshak, M. Mihov, D. Sutton, A. Arshak and S. B. Newcomb, *Microelectron. Eng.*, 2003, **67**–**68**, 130–139.
22 K. Kasahara, C. K. Ober, H. Xu, V. Kosma and J. Odent, *J. Micro/Nanolithography, MEMS, MOEMS*, 2017, **16**, 1.
23 C. Y. Ouyang, Y. S. Chung, L. Li, M. Neisser, K. Cho, E. P. Giannelis and C. K. Ober, in *Advances in Resist Materials and Processing Technology XXX*, ed. M. H. Somervell, 2013, vol. 8682, p. 86820R.
24 C. K. Ober, M. Trikeriotis, S. Chakrabarty, C. Ouyang, M. Kryask and E. P. Giannelis, *J. Photopolym. Sci. Technol.*, 2013, **26**, 659–664.
25 L. Li, S. Chakrabarty, J. Jiang, B. Zhang, C. Ober and E. P. Giannelis, *Nanoscale*, 2016, **8**, 1338–1343.
26 P. G. Reddy, N. Mamidi, P. Kumar, S. K. Sharma, S. Ghosh, K. E. Gonsalves and C. P. Pradeep, *RSC Adv.*, 2016, **6**, 67143–67149.
27 E. C. Mattson, Y. Cabrera, S. M. Rupich, Y. Wang, K. A. Oyekan, T. J. Mustard, M. D. Halls, H. A. Bechtel, M. C. Martin and Y. J. Chabal, *Chem. Mater.*, 2018, **30**, 6192–6206.
28 M. Sortland, J. Hotalen, R. Del Re, J. Passarelli, M. Murphy, T. S. Kulmala, Y. Ekinci, M. Neisser, D. A. Freedman and R. L. Brainard, *J. Micro/Nanolithography, MEMS, MOEMS*, 2015, **14**, 043511.
29 M. Murphy, S. Grzeskowiak, J. Sitterly, G. H. Denbeaux and R. L. Brainard, 2018, **1058608**, 7.
30 M. Murphy, A. Narasimhan, S. Grzeskowiak, J. Sitterly, P. Schuler, J. Richards, G. Denbeaux and R. L. Brainard, *Extrem. Ultrav. Lithogr. VIII*, 2017, **10143**, 1014307.
31 S. Grzeskowiak, A. Narasimhan, M. Murphy, L. Napolitano, D. A. Freedman, R. L. Brainard and G. Denbeaux, *Adv. Patterning Mater. Process. XXXIV*, 2017, **10146**, 1014605.
32 J. Haitjema, Y. Zhang, M. Vockenhuber, D. Kazazis, Y. Ekinci and A. M. Brouwer, in *Extreme Ultraviolet (EUV) Lithography VIII*, eds. E. M. Panning and K. A. Goldberg, 2017, vol. 10143, p. 1014325.
33 J. Haitjema, T. A. Jung, D. Kazazis, A. M. Brouwer, Y. Ekinci, M. Vockenhuber, M. Baljozovic and Y. Zhang, *J. Photopolym. Sci. Technol.*, 2018, **31**, 249–255.
34 D. J. Webb and M. Hatzakis, *J. Vac. Sci. Technol.*, 1979, **16**, 2008–2013.
35 K. Yamaguchi, *J. Electrochem. Soc.*, 1992, **139**, L33.
36 M. Nedelcu, M. S. M. Saifullah, D. G. Hasko, A. Jang, D. Anderson, W. T. S. Huck, G. A. C. Jones, M. E. Weiland, D. J. Kang and U. Steiner, *Adv. Funct. Mater.*, 2010, **20**, 2317–2323.
37 K. R. V Subramanian, M. S. M. Saifullah, E. Tapley, D. J. Kang, M. E. Welland and M. Butler, *Nanotechnology*, 2004, **15**, 158–162.
38 M. S. M. Saifullah, K. R. V Subramanian, E. Tapley, D. J. Kang, M. E. Welland and M. Butler, *Nano Lett.*, 2003, **3**, 1587–1591.
39 M. S. M. Saifullah, M. Z. R. Khan, D. G. Hasko, E. S. P. Leong, X. L. Neo, E. T. L. Goh, D. Anderson, G. a. C. Jones and M. E. Welland, *J. Vac. Sci. {&} Technol. B Microelectron. Nanom. Struct.*, 2010, **28**, 90.
40 K. R. V Subramanian, M. S. M. Saifullah, E. Tapley, D.-J. Kang, M. E. Welland and M. Butler, *Nanotechnology*, 2004, **15**, 158–162.
41 M. S. M. Saifullah, H. Namatsu, T. Yamaguchi, K. Yamazaki and K. Kurihara, *1999 Int. Microprocess. Nanotechnol. Conf.*, 1999, **38**, 160–161.
42 M. S. M. Saifullah, D.-J. Kang, K. R. V. Subramanian, M. E. Welland, K. Yamazaki and K. Kurihara, *J. Sol-Gel Sci. Technol.*, 2004, **29**, 5–10.
43 M. S. M. Saifullah, K. R. V. Subramanian, D. Anderson, D.-J. Kang, W. T. S. Huck, G. A. C. Jones and M. E. Welland, *J. Vac. Sci. Technol. B Microelectron. Nanom. Struct.*, 2006, **24**, 1215.
44 M. S. M. SAIFULLAH, *Cosmos*, 2009, **05**, 1–21.
45 M. S. M. Saifullah, K. R. V Subramanian, D.-J. Kang, D. Anderson, W. T. S. Huck, G. A. C. Jones and M. E. Welland, *Adv. Mater.*, 2005, **17**, 1757–1761.
46 E. Zanchetta, G. Della Giustina, G. Grenci, A. Pozzato, M. Tormen and G. Brusatin, *Adv. Mater.*, 2013, **25**, 6261–6265.
47 L. Brigo, A. Pistore, G. Grenci, A. Carpentiero, F. Romanato and G. Brusatin, *Microelectron. Eng.*, 2010, **87**, 947–950.
48 G. Grenci, G. Della Giustina, A. Pozzato, E. Zanchetta, M. Tormen and G. Brusatin, *Microelectron. Eng.*, 2012, **98**, 134–137.
49 G. Grenci, G. Della Giustina, A. Pozzato, G. Brusatin and M. Tormen, *Microelectron. Eng.*, 2011, **88**, 1964–1967.
50 A. Cattoni, D. Mailly, O. Dalstein, M. Faustini, G. Seniutinas, B. Rösner and C. David, *Microelectron. Eng.*, 2018, **193**, 18–22.
51 R. P. Oleksak, R. E. Ruther, F. Luo, K. C. Fairley, S. R. Decker, W. F. Stickle, D. W. Johnson, E. L. Garfunkel, G. S. Herman and D. A. Keszler, *ACS Appl. Mater. Interfaces*, 2014, **6**, 2917–2921.
52 R. P. Oleksak and G. S. Herman, in *Proc. of SPIE*, eds. O. R. Wood and E. M. Panning, 2014, vol. 9048, p. 90483H.
53 B. Cui, A. S. Abbas, B. B. Shokouhi, S. Alqarni and M. Yavuz, *Mater. Res. Express*, 2014, **1**, 045102.
54 J. Zhang, K. Cao, X. S. Wang and B. Cui, *Chem. Commun.*, 2015, **51**, 17592–17595.
55 S. Il Lee, J. H. Sim, H. J. Lee, R. Kasica, H. M. Kim, C. L. Soles, K. B. Kim and D. Y. Yoon, *Appl. Organomet. Chem.*, 2013, **27**, 644–651.
56 G. Grenci, E. Zanchetta, A. Pozzato, G. Della Giustina, G. Brusatin and M. Tormen, *Appl. Mater. Today*, 2015, **1**, 13–19.
57 M. Zhao, B. Chen, C. Xie, M. Liu and J. Nie, *2010 IEEE 5th Int. Conf. Nano/Micro Eng. Mol. Syst. NEMS 2010*, 2010, 1021–1024.
58 G. Singh, P. Stenberg, P. Vahima, M. Kuittinen, R. P. Yadav and V. Janyani, *Adv. Fabr. Technol. Micro/Nano Opt. Photonics IV*, 2011, **7927**, 792715.
59 A. E. Grigorescu and C. W. Hagen, *Nanotechnology*, 2009, **20**, 292001.
60 A. E. Grigorescu, M. C. van der Krogt, C. W. Hagen and P. Kruit, *Microelectron. Eng.*, 2007, **84**, 822–824.
61 D. A. Czaplewski and L. E. Ocola, *J. Vac. Sci. Technol. B, Nanotechnol. Microelectron. Mater. Process. Meas. Phenom.*, 2011, **29**, 021601.
62 D. A. Czaplewski, D. R. Tallant, G. A. Patrizi, J. R. Wendt and B. Montoya, *J. Vac. Sci. Technol. B Microelectron. Nanom. Struct.*, 2009, **27**, 581.
63 S. Thoms and D. S. Macintyre, *J. Vac. Sci. Technol. B, Nanotechnol. Microelectron. Mater. Process. Meas. Phenom.*, 2014, **32**, 06FJ01.
64 M. Schirmer, B. Büttner, F. Syrowatka, G. Schmidt, T. Köpnick and C. Kaiser, *29th Eur. Mask Lithogr. Conf.*, 2013, **8886**, 88860D.

This journal is © The Royal Society of Chemistry 2019

Please do not adjust margins

65 A. Gerardino, M. Gentili, E. Di Fabrizio, R. Calarco and L. Mastrogiacomo, *Microelectron. Eng.*, 1999, **46**, 201–204.
66 S. Kaya, F. Rahman, D. J. Carbaugh, S. G. Pandya and J. T. Wright, *Nanotechnology*, 2017, **28**, 455301.
67 S. Yasin, D. G. Hasko and H. Ahmed, *Microelectron. Eng.*, 2002, **61**–**62**, 745–753.
68 S. Gorelick, V. A. Guzenko, J. Vila-Comamala and C. David, *Nanotechnology*, , DOI:10.1088/0957-4484/21/29/295303.
69 Y. Chen, D. Macintyre and S. Thoms, *J. Vac. Sci. Technol. B Microelectron. Nanom. Struct.*, 2002, **17**, 2507.
70 W. Hu, G. H. Bernstein, K. Sarveswaran and M. Lieberman, *Proc. IEEE Conf. Nanotechnol.*, 2003, **2**, 602–605.
71 K. Koshelev, M. Ali Mohammad, T. Fito, K. L. Westra, S. K. Dew and M. Stepanova, *J. Vac. Sci. Technol. B, Nanotechnol. Microelectron. Mater. Process. Meas. Phenom.*, 2011, **29**, 06F306.
72 V. R. Manfrinato, A. Stein, L. Zhang, C. Y. Nam, K. G. Yager, E. A. Stach and C. T. Black, *Nano Lett.*, 2017, **17**, 4562–4567.
73 C. Zhang, C. Yang and D. Ding, *J. Micromechanics Microengineering*, 2004, **14**, 663–666.
74 B. Smith, P. Zimmerman, B. Baylav, R. Yin, T. Smith, C. Scholz, P. Xie and M. Zhao, *Adv. Resist Mater. Process. Technol. XXVII*, 2010, **7639**, 763915.
75 M. Wang, N. D. Jarnagin, C. T. Lee, C. L. Henderson, W. Yueh, J. M. Roberts and K. E. Gonsalves, *J. Mater. Chem.*, 2006, **16**, 3701–3707.
76 R. D. Peters, G. R. Amblard, J.-J. Lee and T. Guenther, *Adv. Resist Technol. Process. XX*, 2003, **5039**, 393.
77 A. Subramanian, N. Tiwale and C.-Y. Nam, *JOM*, 2019, **71**, 185–196.
78 Y.-C. Tseng, Q. Peng, L. E. Ocola, D. A. Czaplewski, J. W. Elam and S. B. Darling, *J. Mater. Chem.*, 2011, **21**, 11722.
79 Y. C. Tseng, A. U. Mane, J. W. Elam and S. B. Darling, *Adv. Mater.*, 2012, **24**, 2608–2613.
80 A. Subramanian, G. Doerk, K. Kisslinger, D. H. Yi, R. B. Grubbs and C.-Y. Nam, *Nanoscale*, 2019, **11**, 9533–9546.
81 M. Biswas, J. A. Libera, S. B. Darling and J. W. Elam, *Chem. Mater.*, 2014, **26**, 6135–6141.
82 L. Y. M. Tobing, L. Tjahjana and D. H. Zhang, *Nanotechnology*, 2013, **24**, 075303.
83 Y. Ozaki, S. Ito, N. Hiroshiba, T. Nakamura and M. Nakagawa, *Jpn. J. Appl. Phys.*, , DOI:10.7567/JJAP.57.06HG01.
84 M. Kulsreshath, A. Vital, P. Lefaucheux, C. Sinturel, T. Tillocher, M. Vayer, M. Boufnichel and R. Dussart, *Micro Nano Eng.*, 2018, **1**, 42–48.
85 B. Wu, A. Kumar and S. Pamarthy, *J. Appl. Phys.*, 2010, **108**, 051101.
86 K. J. Dusoe, X. Ye, K. Kisslinger, A. Stein, S. W. Lee and C. Y. Nam, *Nano Lett.*, 2017, **17**, 7416–7423.
87 R. L. Brainard, M. Neisser, G. M. Gallatin and A. K. Narasimhan, in *EUV Lithography, Second Edition*, SPIE, 2018, pp. 493–591.
88 R. Fallica, J. Haitjema, L. Wu, S. Castellanos, A. M. Brouwer and Y. Ekinci, *J. Micro/Nanolithography, MEMS, MOEMS*, 2018, **17**, 1.
89 R. Fallica, J. Haitjema, L. Wu, S. Castellanos, F. Brouwer and Y. Ekinci, in *Extreme Ultraviolet (EUV) Lithography VIII*, eds. E. M. Panning and K. A. Goldberg, 2017, vol. 10143, p. 101430A.
90 J. Kamcev, D. S. Germack, D. Nykypanchuk, R. B. Grubbs, C. Y. Nam and C. T. Black, *ACS Nano*, 2013, **7**, 339–346.
91 Q. Peng, Y. C. Tseng, Y. Long, A. U. Mane, S. DiDona, S. B. Darling and J. W. Elam, *Langmuir*, 2017, **33**, 13214–13223.
92 X. Ye, J. Kestell, K. Kisslinger, M. Liu, R. B. Grubbs, J. A. Boscoboinik and C. Y. Nam, *Chem. Mater.*, 2017, **29**, 4535–4545.
93 L. E. Ocola, A. Connolly, D. J. Gosztola, R. D. Schaller and A. Yanguas-Gil, *J. Phys. Chem. C*, 2017, **121**, 1893–1903.
94 C. Z. Leng and M. D. Losego, *Mater. Horizons*, 2017, **4**, 747–771.
95 C.-Y. Nam and A. Stein, *Adv. Opt. Mater.*, 2017, **5**, 1700807.
96 J. J. Kim, H. S. Suh, C. Zhou, A. U. Mane, B. Lee, S. Kim, J. D. Emery, J. W. Elam, P. F. Nealey, P. Fenter and T. T. Fister, *Nanoscale*, 2018, **10**, 3469–3479.

This journal is © The Royal Society of Chemistry 2019

Please do not adjust margins

The table of contents entry

Advancing the next generation nanolithography with infiltration synthesis of hybrid nanocomposite resists

Nikhil Tiwale, Ashwanth Subramanian, Kim Kisslinger, Ming Lu, Jiyoung Kim, Aaron Stein, and Chang-Yong Nam *

Novel positive-tone hybrid resists developed by vapor-phase inorganic infiltration feature fully tunable resist performance parameters and high-aspect-ratio pattern transfer capability.

Keywords: *Hybrid nanocomposite resist, infiltration synthesis, electron beam lithography, high aspect ratio pattern transfer, cryogenic silicon etch*